**Advances in Nano Research**, *Vol. 17, No.5 (2024) 473-485*
https://doi.org/10.12989/anr.2024.17.5.473


# Green synthesis of potassium silicate nanoparticles from biomass ashes and their antimicrobial potential

Abhishek Sharma[1], Anirudh kumar[1], Vikas Kumar[1], Garima Sharma[2], Vini Madathil[3], DVN Sudheer Pamidimari[3], Beer Pal Singh[1], Satendra Pal Singh[4], Ashish Ranjan Sharma[*5] and Sanjeev Kumar Sharma[**1]

[1]*Biomaterials and Sensor Laboratory, Department of Physics, Ch. Charan Singh University, Meerut, Uttar Pradesh-250004, India*
[2]*Department of Biomedical Science & Institute of Bioscience and Biotechnology, Kangwon National University, Chuncheon 24341, Republic of Korea*
[3]*Department of Molecular Biology and Genetics, Gujarat Biotechnology University, Gandhinagar, Gujarat- 382355, India*
[4]*Department of Physics, S.S.V. College, (Affl. CCS University, Meerut), Hapur, Uttar Pradesh-245101, India*
[5]*Institute for Skeletal Aging & Orthopedic Surgery, Hallym University, Chuncheon Sacred Heart Hospital, Chuncheon-si 24252, Gangwon-do, Republic of Korea*

(*Received May 27, 2024, Revised September 28, 2024, Accepted October 16, 2024*)

**Abstract.** Biogenic potassium silicate ($K_2SiO_3$) NPs were synthesized from the biomasses of walnut shell (w-$K_2Si$), pinewood stem (p-$K_2SiO_3$), and sugarcane bagasse (s-$K_2SiO_3$) by ambient fiery and KOH-assisted thermal process. The crystallite size (*D*) of w-$K_2SiO_3$, p-$K_2SiO_3$, and s-$K_2SiO_3$ NPs were determined to be 73 nm, 53 nm and 47 nm using Debye-Scherrer's formula. The varied strain of all samples was observed in the 0.284 to 0.301 range. Microstructure showed the cubical geometry with an irregular grain size of $K_2SiO_3$ NPs, while the SAED pattern confirmed the polycrystalline nature. The $E_g$ of w-$K_2SiO_3$, p-$K_2SiO_3$, and s-$K_2SiO_3$ NPs was determined from Tauc's plot to be 3.66 eV, 3.75 eV, and 3.78 eV, which are closely matched to be 3.78 eV, 3.88 eV, and 3.79 eV estimated from the XPS core-level analysis. The antibacterial activity of w-$K_2SiO_3$, p-$K_2SiO_3$, and s-$K_2SiO_3$ NPs was investigated against *E. coli* and *S. aureus* bacteria. Compared to $K_2SiO_3$ NPs, the s-$K_2SiO_3$ were found to be highly toxic against *E. coli* and *S. aureus* and completely inhibited the growth of both organisms within 6 h. The findings represent the novel low-cost development of $K_2SiO_3$ NPs with potent antibacterial activities.
**Keywords:** antimicrobial activity; bandgap engineering; microstructural analysis; potassium silicate ($K_2SiO_3$) nanoparticles (NPs); residual stress from W-H model

## 1. Introduction

Silicates are pioneering antimicrobial agents against the broad spectrum of gram-positive or gram-negative microbes due to favorable surface chemistry and amazing cell-viable nanomaterial owing to decent biocompatibility [1, 2]. Generally, silicates [$M_x(SiO_{2+n})^{2n-}$] occur as inorganic compounds consisting of subunits; silicate anions $(SiO_{2+n})^{2n-}$ typically associated with charge-balancing metal cations $M_x$ ($Mg^{2+}$, $Ca^{2+}$, $Fe^{2+}$, $Na^+$, and $K^+$), and are found most abundant in the earth's crust by mass (95%) (Mason 1966). Potassium silicate ($K_2SiO_3$) is one of the most important members of the silicate family, which effectively attributes high surface functionalization, and their textural along with multimodal porosity engineering has a great potential to achieve an outstanding level of maturity (Gandolfi *et al*. 2008; Wu *et al*. 2015). Potassium (K) is an essential nutrient for plants, and the most abundant cation found consistently with the apoplastic concentration in the cytoplasm between 100 to 200 mm that helps plants to regulate water uptake, enzyme activation, photosynthesis, protein synthesis, osmoregulation, stomatal movement, phloem transport, energy transfer, cation-anion balance, and stress resistance (Wang *et al*. 2013, Danchin and Nikel 2019). Meanwhile, phytogenic silica supports plants' growth, strengthens against biotic/abiotic stress and health, and improves plant water/mineral uptake capacity (Deshmukh *et al*. 2017). It also provides a defense mechanism against pests and heavy metal toxicity, including soil salinity, and alleviates immunity regarding diseases (Bhat *et al*. 2019). In animals, $K^+$ is a critical electrolyte that assists nerves to function and muscles to contract, ensuring optimal water balance and pH within the system (He and MacGregor 2008). It also helps to move nutrients into cells and waste products out of cells. In addition, it maintains essential cardiovascular functions, such as maintaining regular heartbeat, blood pressure, and metabolizing carbohydrates (Tannen 1983).

Similarly, silica in animals remarkably functions in organs and connective tissue via collagen cross-linking. Moreover, it is also well-known for strengthening bone tissues (Carlisle 1986). Various methods to synthesize silicate micro and nanostructures and their biological activities have been studied. For example, Oliveira *et al*. (2022) synthesized silicate microstructures and cooperative formation of inorganic-organic interfaces. In addition, Li *et*

*Corresponding author, Ph.D.,
E-mail: researchskeletal@gmail.com
**Co-corresponding author, Ph.D.,
E-mail: sksharma18@ccsuniversity.ac.in



ISSN: 2287-237X (Print), 2287-2388 (Online)

*al*. (2019) synthesized ATO/$K_2SiO_3$ film prepared by twice-sprayed pyrolysis, and their hydrophilic, anticorrosive, thermal conductive, and electrical resistive properties were studied. Walker and Whitehead (1966) also prepared $K_2SiO_3$ liquors of composition ($SiO_2/K_2O$) with ratios of 4:1 from aerosil, acidic washed silica-gel fines or potash glass and studied by (I) light scattering, (II) reaction with molybdate and (III) usage of the metachromatic effect with pinacyanol chloridse. Mastalska-Poplawska *et al*. (2020) synthesized transparent and intumescent polymer-silicate hydrogels by free-radical polymerization in the presence of cross-linking monomer (N,N′-methylenebisacrylamide) with the redox initiators system (potassium persulphate/ sodium thiosulphate). They examined rheologically at different sodium acrylate concentrations to study enhanced fire-retardant properties with the development of intumescent hydrogels. Another study to synthesize $K_2SiO_3$ from potassium carbonate and calcium silicate was reported by Wu and Liu (2007), which also reported the rate of releasing $K_2SiO_3$ fertilizer as a functioning superabsorbent and for water retention application. Menzies *et al*. (1992) have reported the foliar applications of $K_2SiO_3$ to reduce the severity of powdery mildew on cucumber, muskmelon, and zucchini squash and tested the persistence of Si foliar sprays on cucumber. Conventionally, fly ashes collected from the molten ashes serve as one of the basic raw materials for manufacturing $K_2SiO_3$ (Hongwen *et al*. 2015). Commercially available synthetic sources of silica, such as tetraethyl orthosilicate (tetraethoxysilane or TEOS), ethyl silicate $Si(OC_2H_5)_4$, and silicic acid are employed to synthesize $K_2SiO_3$. However, these commercial resources are impractical in the industries owing to their high cost and harmful effects on health/environment. It is consequently imperative to find a new, safer, more economical, and environmentally acceptable source of $K_2SiO_3$. Biomass waste is produced abundantly every year and it has been found that biomass waste contains a high silica concentration, which can be used as an alternative raw material for the development of $K_2SiO_3$ (Permatasari *et al*. 2016, França *et al*. 2017).

Comparatively, biomass-derived $K_2SiO_3$ displays an extraordinary advantage over synthetic potassium silicate in the sense of its nontoxic behavior, tuneable microstructure, and cost-effectiveness, as well as eco-friendly methods of synthesis (Mughal *et al*. 2021). Furthermore, diversified forms of $K_2SiO_3$ NPs can be synthesized from compositionally different raw biomasses from different silicon/silica sources, viz. phytoliths, sponge spicules, diatoms, including radiolarian and potassium sources (Imran *et al*. 2020, Nandiyanto *et al*. 2017, Hongwen *et al*. 2015, de Oliveira *et al*. 2022, Kumchompoo and Puntharod 2022). Moreover, the micro-structure of synthesized $K_2SiO_3$ NPs can be further tuned by varying the physical and chemical conditions *via* different synthesis approaches (Hu *et al*. 2015). Nandiyanto *et al*. (2017) synthesized $K_2SiO_3$ NPs from rice straw ash using a flame-assisted spray-pyrolysis method at 700 °C for 3 h using. Consequently, biogenic $K_2SiO_3$ has a future prominent potential in versatile in-vitro/in-vivo medical applications, such as antibacterial activity, intelligent drug delivery and release systems, bone tissue implantation, cancer therapeutic, and bioimaging/sensing (Tallury *et al*. 2008, Jurkić *et al*. 2013, Zhu *et al*. 2017, Venkatraman and Swamiappan 2020, Ghiasi Moaser *et al*. 2023). Distinctive topographies of biogenic $K_2SiO_3$ and its subunits, potassium ($K^+$) and silicate $(SiO_3)^{2-}$ ions, imply to attire multiple biomedical significance, which play a pivotal role in the cell culture of plant and animal cells (Jones and Handreck 1967, Epstein 2009, Wang *et al*. 2013, Dogan *et al*. 2019, Pandey and Mahiwal 2020).

The KOH-assisted thermal process has recently been employed to produce activated carbon (Xu *et al*. 2017, Jawad and Abdulhameed 2020, Ao *et al*. 2021). Various researchers have reported the synthesis of carbon-based nanomaterials such as graphene, graphene oxide, and reduced graphene oxide by KOH-assisted thermal/ microwave process (Deng *et al*. 2018, Kang *et al*. 2019, Tamuly *et al*. 2022, Youssry *et al*. 2023). This innovative approach of the KOH-assisted thermal process utilizes biomass waste for sustainable material synthesis and demonstrates the versatility of KOH-assisted thermal processes in producing advanced nanocomposite materials (Tamuly *et al*. 2022). The synthesis of biogenic $K_2SiO_3$ NPs *via* ambient fiery and KOH-assisted thermal processes and their antimicrobial response is a novel study and has not been reported to date.

In this work, we have demonstrated a simple chemical-free approach to synthesize biogenic $K_2SiO_3$ NPs, i.e., w-$K_2SiO_3$, p-$K_2SiO_3$, and s-$K_2SiO_3$, from three different types of biomass ashes, i.e. walnut shell (WS), pinewood stem (PS), and sugarcane bagasse (SB), respectively. The micro-structure of w-$K_2SiO_3$, p-$K_2SiO_3$, and s-$K_2SiO_3$ NPs could be controlled by crushing biomass ash and subsequently varying annealing temperature at 700 °C for different time intervals (Pascal *et al*. 1999, Zeng *et al*. 2007). The microstructure of $K_2SiO_3$ NPs also depends on several factors such as soil, soil microbial species, soil pH, geographical location, and environmental conditions of the production land of biomass (Van Horn *et al*. 2013). The microstructural, mechanical, elemental, optical, and electrical properties along with the chemical bonding of $K_2SiO_3$, were evaluated by using X-ray diffractometer (XRD), field emission-scanning electron microscopy (FE-SEM), high resolution-scanning electron microscopy (HR-TEM), surface area energy dispersion (SAED) patterns, UV-Vis spectroscopy, and X-ray photoelectron spectroscopy (XPS), respectively. The synthesis mechanism of $K_2SiO_3$ NPs from biomass wastes is also discussed. Furthermore, the antibacterial activity of w-$K_2SiO_3$, p-$K_2SiO_3$, and s-$K_2SiO_3$ NPs was investigated against *Escherichia coli* (*E. coli*) and *Staphylococcus aureus* (*S. aureus*). In our study, the synthesized s-$K_2SiO_3$ NPs were highly toxic against *E. coli* and *S. aureus* compared to p-$K_2SiO_3$ and w-$K_2SiO_3$ NPs. The s-$K_2SiO_3$ NPs completely inhibited the growth of both microorganisms within 6 h of treatment. The findings reveal a novel low-cost synthesis of $K_2SiO_3$ NPs with potent antibacterial activities.

## 2. Experimental

### *2.1 Materials and methods*

Biomass, such as pinewood stem (PS), sugarcane bagasse (SB), and walnut shell (WS), were collected from

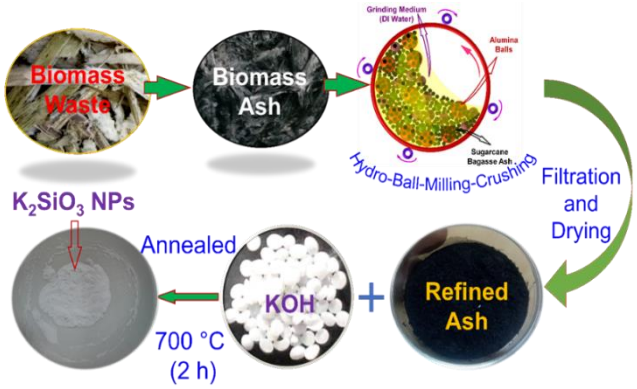


Fig. 1 Schematic diagram of chemical-free (green) synthesis of $K_2SiO_3$ NPs from biomass waste.

local markets in west UP, India. All chemicals and solvents of AR grade were purchased from Merck and Sigma Aldrich (India) and used without further purification.

### *2.2 Synthesis of biogenic potassium silicate*

Biogenic w-$K_2SiO_3$, p-$K_2SiO_3$, and s-$K_2SiO_3$ NPs were synthesized *via* a chemical-free approach through ambient fiery and KOH-assisted thermal process. The synthesis of $K_2SiO_3$ NPs from biomass wastes is shown by a schematic representation (Fig. 1). Initially, biomasses of WS, PS, and SB, were washed with tap water to remove environmental dust particles and undesired contaminations, then rinsed with deionized (DI) water to remove the tap water contaminations and finally dried at 80 °C for 12 h in a hot air oven. Then, WS, PS, and SB were ambiently burnt using the fire-burning gas nozzle, and their ashes were obtained, i.e., WSA, PSA, and SBA, respectively. The burnt black ashes of these three biomasses were finely crushed in DI water by ball milling at room temperature for 10 h. The finally crushed ashes were then filtered with the help of Whatman paper of grade 1 (110 mm, 1111 µm) using the funnels and washed with a large amount of DI water. Hydro-ball-milling crushing and filtration removes heavy metal ions such as $Fe^{2+}$, $Cu^{2+}$, and $Al^{3+}$ from the ashes. The obtained precipitates were dried in a hot air oven at 60 °C for 1 h to detach the filter paper from the funnel and then dried at 80 °C for 2 h to separate the filtrate ashes from the filter papers. All three washed and filtered black ashes were finally dried at 100 °C for 3 h. Then, the dried ashes were stored and sealed in the borosil vials. 1 g of each of all three prepared materials was mixed with 3 g of KOH, crushed separately with agate mortar's help for 5 min, and then transferred into three different alumina crucibles. All three samples were annealed at 700 °C for 2 h in a muffle furnace at the heating ramp rate of 5 °C per minute. The synthesized biomass-derived $K_2SiO_3$ NPs were naturally cooled to room temperature.

### *2.3 Characterization of the $K_2SiO_3$ nanopowders*

The surface morphology of synthesized w-$K_2SiO_3$, p-$K_2SiO_3$, and s-$K_2SiO_3$ NPs was determined by FE-SEM (Hitachi, S-4800) and BF-TEM. The Au was sputtered on the surface of $K_2SiO_3$ samples to avoid the charging effect using JEOL Auto Fine Coater (JEC-3000FC) at 30 A for 40 sec. The microstructural properties of all types $K_2SiO_3$ NPs were investigated *via* Panalytical X-ray diffractometer (XRD) (X'Pert3 Powder) using a CuKα1 radiation source (λ = 1.5405 Å) under a constant current of 40 mA at 40 kV and with a scan range of 10–80°. The crystallinity of the nanopowders were analyzed using XRD pattern (Kumar *et al*. 2013, Bogireddy *et al*. 2017), and further justified by the SAED pattern. A Phoibos 100 hemispherical energy analyzer (PHOIBOS 100-63 MCD) took the typical XPS survey of w-$K_2SiO_3$, p-$K_2SiO_3$, and s-$K_2SiO_3$ NPs in a constant analyzer energy (CAE) mode (Specs GmbH, Berlin, Germany: Mg radiation source 1253.6 eV, and 125W power). The overall resolution of 0.9 eV was measured and calibrated using the Ag $3d_{5/2}$ (368.3 eV) and Au $4f_{7/2}$ (84.0 eV) signals. The base pressure in an analysis chamber was kept to be $5\times10^{-10}$ mbar. Before recording the data, the sample was degassed in a vacuum overnight. The optical properties of $K_2SiO_3$ NPs were evaluated from the microprocessor-controlled UV–Vis double beam spectrophotometer (Model: IG-27DS) in the 190 -850 nm range.

### *2.4 Antimicrobial studies*

Two distinct pathogenic species of *E. coli* (gram-negative) and *S. aureus* (gram-positive) as representative organisms bacterial strains were used in the antibacterial activity of $K_2SiO_3$ NPs. *S. aureus* and *E. coli* organisms were cultured in a Luria-Bertani (LB) nutritional medium at 37 °C overnight. These culture plates were filled with 0.1 mg $mL^{-1}$ of the w-$K_2SiO_3$, p-$K_2SiO_3$, and s-$K_2SiO_3$ NPs. In order to confirm that the material's toxicity caused the decline in colony-forming units (CFU), a control sample was kept without NPs treatment and evaluated in parallel with the experiment. For both *E. coli* and *S. aureus*, the CFU change per mL was computed *via* respective colony counting at an interval of 1 h and compared with the control.

## 3. Results and discussion

### *3.1 Microstructural analysis*

The crystal structure, phase formation, and crystallite size of w-$K_2SiO_3$, p-$K_2SiO_3$, and s-$K_2SiO_3$ NPs were determined by the XRD. Fig. 2(a) show the XRD pattern traced between 20° and 60° at scan rate of 1° per min for all samples of $K_2SiO_3$ NPs. Peak profile analysis of all samples indicates a rare combination of potassium and silica. The observed XRD pattern has been compared with reference data of JCPDS file #84-0366 (Fig. 2(a)), which confirms the polycrystalline structure of all samples ($K_2SiO_3$ NPs). The XRD pattern with sharp peak profile of all samples was observed at 25.65, 26.94, 29.52, 30.69, 32.10, 32.62, 35.20, 38.60, and 41.40 corresponding to planes (131), (130), (113), (214), (140), (200), (225), (221), and (231), respectively. The dominant peak (113) of $K_2SiO_3$ NPs was observed at 29.52 in all samples. The intensity of various

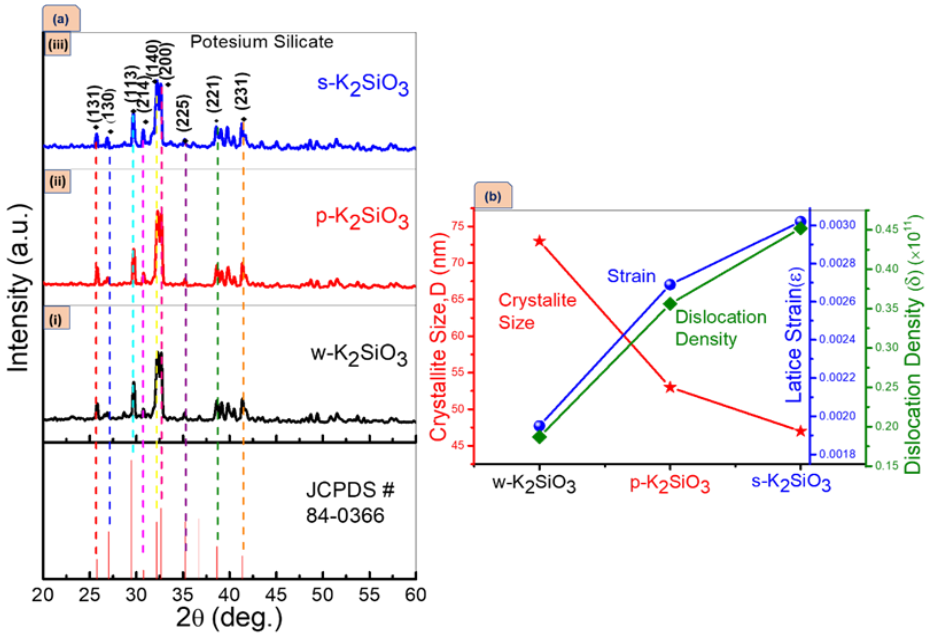


Fig. 2 (a) XRD pattern, and (b) Crystallite size, lattice strain and dislocation density determination of w-$K_2SiO_3$, p-$K_2SiO_3$, and s-$K_2SiO_3$ NPs using Debye-Scherrer's formula

peaks deteriorated due to the partial amorphization and formation of grain boundaries. The crystallite size (d) of w-$K_2SiO_3$, p-$K_2SiO_3$, and s-$K_2SiO_3$ NPs were calculated as 73 nm, 53 nm, and 47 nm, respectively, using Debye-Scherrer's formula, which is as follows:

$$d = \frac{k\lambda}{\beta_{hkl}\cos\theta} \quad (1)$$

where $k$ is denoted as the material's constant ($k$=0.89), $\beta_{hkl}$ is the FWHM of the diffraction peak at angle $\theta$, and $\lambda$ is the wavelength of X-ray corresponding to CuK$\alpha_1$ ($\lambda$=0.1540 nm) radiation under a constant current of 40 mA at a potential difference of 40 kV. The diffraction patterns of these three samples were achieved equally in structure. Compared to w-$K_2SiO_3$ NPs, a slight decrease in the peak intensity was observed for p-$K_2SiO_3$ and s-$K_2SiO_3$ NPs, which is inappropriate for distinguishing d-spacing of silicate molecules because of different distributions of moisture content in materials. The decrease in peak intensity of the XRD pattern at 29.59° indicates the absorption of water molecules by the silicate molecules (Billingham *et al*. 1997). Decreasing the peak intensity of p-$K_2SiO_3$ and s-$K_2SiO_3$ NPs, the value of $\beta_{hkl}$ increased, signifying a decrease in the crystallinity, which is correlated to Scherrer's Eq. (1).

The development of lattice strain (ε) in all samples was calculated from the following equation:

$$\varepsilon = \frac{\beta_s}{4\tan\theta_{hkl}} \quad (2)$$

In the XRD section, specify how peak shifts and broadening correlate with particle size and crystallinity changes, particularly in relation to the Debye-Scherrer calculations.

The lattice strain of w-$K_2SiO_3$, p-$K_2SiO_3$, and s-$K_2SiO_3$ NPs was observed as 0.195, 0.269, and 0.302, respectively (Fig. 2(b)). The positive value of the observed strain indicates the identical distance of relevant crystal planes, which might be possible due to the presence of defects and stresses. The following expression was used to estimate the stress along the plane (113):

$$\sigma = Y\varepsilon \quad (3)$$

where $Y$ is the Young's modulus (75 GPa) for $SiO_2$ (Chen *et al*. 2014), and σ is presented as the stress of the material. The strain and stress values of $K_2SiO_3$ NPs extracted from WSA, PSA, and SBA are tabulated in Table 1. The dislocation density ($\delta$) of the samples was calculated by Williamson Smallman's equation:

$$\delta = {}^{n}/_{d^2} \quad (4)$$

Here, $n$ is a fraction of unity, and $d$ is the crystallite size. As per Scherrer's equation, peak broadening for the crystallite size of the materials generally depends on 1/cosθ, whereas the strain of materials depends on tanθ as shown in Eqs. (1) and (2). The contribution of crystallite size and strain in the peak broadening are independent and exhibit a Cauchy-like profile. Therefore, the following relationship can be established by the sum of peak broadening responsible for crystallite size and strain.

$$\beta_{hkl} = [\beta_d + \beta_s] \quad (5)$$

By substituting eq. (1) and (2) put in eq. (5) the value of peak broadening is given by

$$\beta_{hkl} = \left[\frac{k\lambda}{d\cos\theta} + 4\varepsilon\tan\theta\right] \quad (6)$$

Now rearrange the above equation, and we get,

$$\beta_{hkl}\cos\theta = \frac{k\lambda}{d} + 4\varepsilon\sin\theta \quad (7)$$

Table 1 The crystallite size, lattice strain, and dislocation density estimated from the Scherrer and W-H equations of $K_2SiO_3$ NPs derived from PSA, SBA, and WSA biomass ashes

| Samples | Debye-Scherrer's formula | | | | W-H method (UDM) | | |
|---|---|---|---|---|---|---|---|
| | Crystallite Size (nm) | Lattice Strain ε (×$10^{-2}$) | Lattice Stress σ (×$10^{3}$) | Dislocation density δ (×$10^{11}$) $cm^{-2}$ | Crystallite Size (nm) | Lattice Strain ε (×$10^{-2}$) | Dislocation density δ (×$10^{11}$) $cm^{-2}$ |
| w-$K_2SiO_3$ | 73 | 0.195 | 14.62 | 0.187 | 138 | 0.087 | 0.052 |
| p-$K_2SiO_3$ | 53 | 0.269 | 20.17 | 0.356 | 125 | 0.155 | 0.064 |
| s-$K_2SiO_3$ | 47 | 0.302 | 22.65 | 0.452 | 78 | 0.166 | 0.164 |

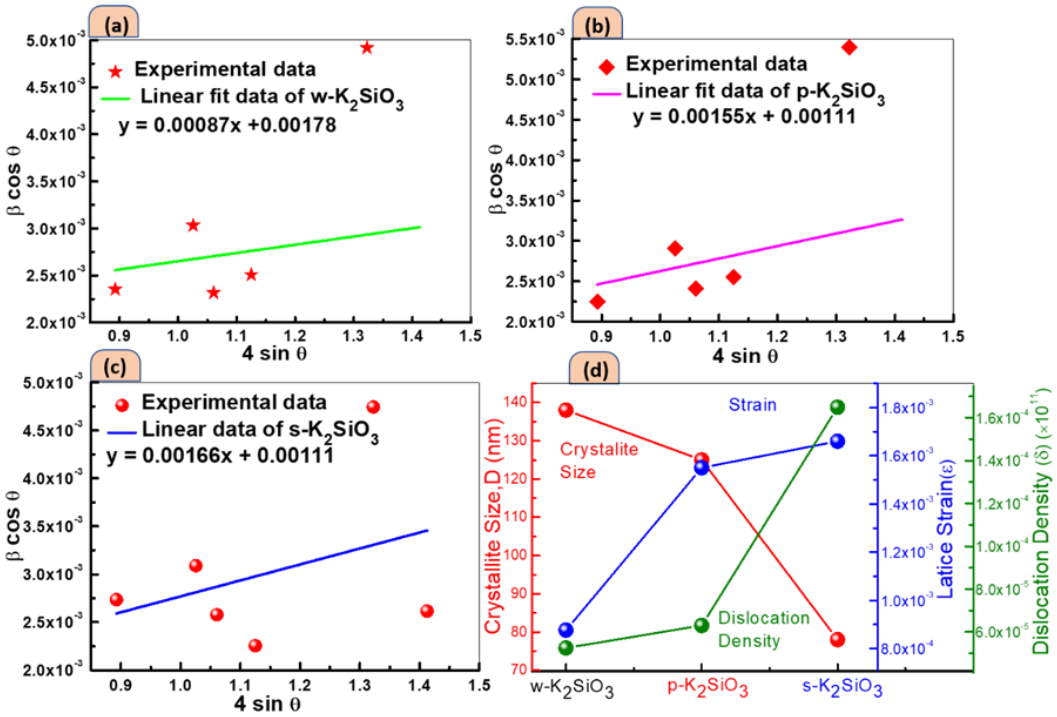


Fig. 3 (a-c) Williamson-Hall equation plot, and (d) crystallite size, lattice strain of w-$K_2SiO_3$, p-$K_2SiO_3$, and s-$K_2SiO_3$ NPs, respectively

The above equation is a straight-line equation known as the Williamson-Hall equation. Figs. 3(a-c) demonstrates the W-H plot of all samples. The crystallite size, strain, and dislocation density of w-$K_2SiO_3$, p-$K_2SiO_3$, and s-$K_2SiO_3$ NPs are shown in Fig. 3(d). According to the result, the crystallite size of all samples of $K_2SiO_3$ was determined to be 138 nm, 125 nm, and 78 nm, respectively, and the strain was observed to be 0.087, 0.155, and 0.166, for w-$K_2SiO_3$, p-$K_2SiO_3$, and s-$K_2SiO_3$ NPs, respectively. The crystallite size estimated from the W-H plot analysis was higher than the crystallite size calculated from Debye-Scherrer's formula, which is possible because the W-H equation considers the broadening phenomenon caused by the internal strain, while Scherrer's method does not (Gong and Kim 2013). Dislocation density ($\delta$) indicates the malformation of the lattice sight compared to the well-arranged crystal lattice of the material. The dislocation density values of w-$K_2SiO_3$, p-$K_2SiO_3$, and s-$K_2SiO_3$ NPs, are shown in Fig. 2(b). The dislocation density of the material can occur due to unlike vacancies, interstitial defects, and point defects, among other things. Table 1 summarises the computed $\delta$ for all biomasses.

Figs. 4(a-c) show the digital images of WS, PS, and SB biomasses and snapshots of their ashes in the corresponding inset, respectively. Figs. 4(d-f) show the FE-SEM images of synthesized w-$K_2SiO_3$, p-$K_2SiO_3$, and s-$K_2SiO_3$ NPs, respectively. The microstructure of p-$K_2SiO_3$ was agglomerated NPs. The other two synthesized nanomaterials (s-$K_2SiO_3$, and w-$K_2SiO_3$) showed non-uniform, asymmetrical, and agglomerated NPs that moderately/ highly adhered with each other. The average crystallite size of w-$K_2SiO_3$, p-$K_2SiO_3$, and s-$K_2SiO_3$ NPs decreased from 138 nm to 78 nm, respectively. BF-TEM images of w-$K_2SiO_3$, p-$K_2SiO_3$, and s-$K_2SiO_3$ NPs are shown in Figs. 4(g-i), respectively. The p-$K_2SiO_3$ showed an agglomerated and asymmetrical geometry with a wide size distribution similar to cubical shapes of approximately 125 nm. Every primary particle was interconnected and adhered to each other. The s-$K_2SiO_3$ and w-$K_2SiO_3$ NPs clearly showed moderately and highly combined NPs with an average crystallite size of 78 nm and 138 nm, respectively. Comparatively, s-$K_2SiO_3$ NPs were observed to be the most minor and non-uniform size distribution of NPs. The SAED pattern of w-$K_2SiO_3$, p-$K_2SiO_3$, and s-$K_2SiO_3$ NPs are shown in the inset of Figs.

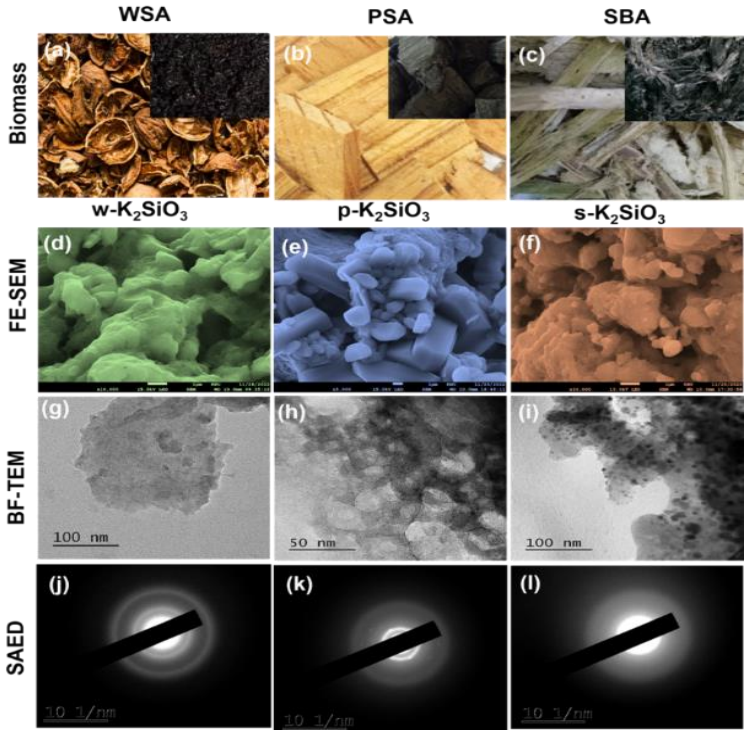


Fig. 4 Surface morphology analysis by biomasses (a, b & c), FE-SEM (d, e & f), BE-TEM, (g, h & i) and SAED patterns (j, k & l) of w-$K_2SiO_3$, p-$K_2SiO_3$, and s-$K_2SiO_3$ NPs

Table 2 Optical band gap, Urbach Energy (eV), and Refractive Index ($\eta$) of w-$K_2SiO_3$, p-$K_2SiO_3$, and s-$K_2SiO_3$ NPs

| Samples | Bandgap energy ($E_g$) (eV) | Urbach Tail ($E_U$) (eV) | Refractive Index ($\eta$) |
|---|---|---|---|
| w-$K_2SiO_3$ | 3.66 | 0.3108 | 1.8148 |
| p-$K_2SiO_3$ | 3.75 | 0.3003 | 1.7528 |
| s-$K_2SiO_3$ | 3.78 | 0.2601 | 1.7404 |

4(j-l), respectively. The electron diffraction rings with tiny dots in all SAED images also indicated the polycrystalline nature of all $K_2SiO_3$ NPs samples.

### *3.2 Optical Properties*

The optical properties such as Urbach tail ($E_U$), bandgap ($E_g$), and refractive index ($\eta$) were determined from the transmittance spectra of WSA, PSA, and SBA-derived $K_2SiO_3$ NPs from UV-Vis spectroscopy. Fig. 5(a) shows the absorption and transmission spectra of biomass-derived $K_2SiO_3$ NPs in the 200 - 850 nm range. The broadened edges of the absorption spectra were observed in the 300-375 nm range. The absorption spectrum of biomass is primarily affected by the roughness, scattering from the surface, oxygen deficit, and impurity centers (Kumar and Mohanty 2014). It is clear from the inset of Fig. 5(a) that the observed average transmittance percentage of w-$K_2SiO_3$, p-$K_2SiO_3$, and s-$K_2SiO_3$ NPs is 22%, 45%, and 43%, respectively. The optical energy bandgap ($E_g$) was determined from Tauc's plot. The trend of $E_g$ of silicate samples is shown in Fig. 5(b). The optimization of $E_g$ for these three biomasses was determined by the intercept value of the plot at the x-axis as photon energy $h\nu$ (eV) vs. $(\alpha h\nu)^n$

$$(\alpha h\nu)^n = C_m(h\nu - E_g) \quad (8)$$

on the y-axis. The Tauc's relation is given in the following equation.

Where $E_g$ is the optical energy bandgap, $h\nu$ is the energy of the incident photon, $\alpha$ is the optical absorption coefficient, and $C_m$ is the material constant. The value of "$n$" in the Tauc's relation depends on the transmission phenomenon. The $E_g$ of biomass-derived $K_2SiO_3$ NPs has been treated as the direct bandgap by applying factor "$n$" as 2. The $E_g$ of w-$K_2SiO_3$, p-$K_2SiO_3$, and s-$K_2SiO_3$ NPs was calculated to be 3.66 eV, 3.75 eV, and 3.78 eV, respectively. The size of particles could significantly influence the $E_g$ of silicates. The higher values of $E_g$ are responsible for the smaller particle size of silicates (Asyikin *et al.* 2020). Fig. 5(c) illustrates the $E_U$, which was created by the straight line of the natural logarithm of the absorption coefficient $ln(\alpha)$ against $(h\nu)$. The $E_U$ of the materials is computed as the inverse slope of a straight line. The $E_U$ informs us about the scale of disorder in amorphous materials (Dousti *et al.* 2013). Materials with high $E_U$ levels are more prone to introduce weak bonds, such as defects (Halimah *et al.* 2010). The $E_U$ of w-$K_2SiO_3$, p-$K_2SiO_3$, and s-$K_2SiO_3$ NPs were estimated to be 0.3108 eV, 0.3003 eV, and 0.2601 eV, respectively (Table 2). The $\eta$ of the materials is another substantial parameter for optical properties that directly depends on the degree of the crystallinity (Sommer *et al.* 2016). The values of $\eta$ are used as the potential of the material for utilization as optical devices (Azlan *et al.* 2014). Using the $E_g$, we have determined the $\eta$ of w-$K_2SiO_3$, p-$K_2SiO_3$, and s-$K_2SiO_3$ NPs

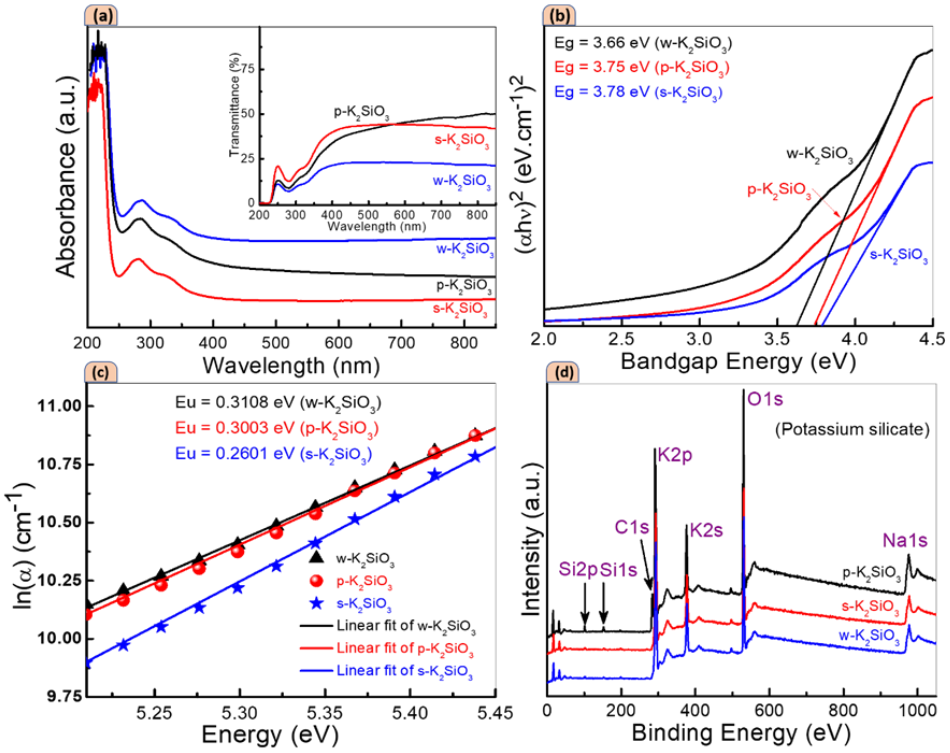


Fig. 5 (a) UV-visible absorption, where the inset shows the transmission spectra, (b) direct bandgap, (c) Urbach energy tail plot, and (d) full survey of XPS spectra of w-$K_2SiO_3$ NPs, p-$K_2SiO_3$ NPs, and s-$K_2SiO_3$ NPs.

by applying the following equation (Reddy *et al*. 1998).

$$n = 4.084 - 0.62E_g \quad (9)$$

Where $E_g$ is the optical bandgap value and $\eta$ is the refractive index. The calculated values of $\eta$ with $E_g$ for w-$K_2SiO_3$, p-$K_2SiO_3$, and s-$K_2SiO_3$ NPs are given in Table 2. It was observed that $\eta$ of all three samples ($K_2SiO_3$ NPs) decreased in the order from 1.8148 to 1.7404.

### *3.3 Elemental analysis and binding energy*

The chemical composition of p-$K_2SiO_3$, s-$K_2SiO_3$, and w-$K_2SiO_3$ NPs was investigated using XPS analysis. The concentration, chemical valence, microstructure, and elemental composition of the top of the surface of the materials could be determined because of the usual sample depth for XPS, which was up to 10 nm. The XPS peak fitting software "XPSPEAK4.1" was used to observe the core-level analysis of p-$K_2SiO_3$, s-$K_2SiO_3$, and w-$K_2SiO_3$ NPs. The XPS complete survey shows the existence of Si, K, fraction part of Na and O atoms in p-$K_2SiO_3$, s-$K_2SiO_3$, and w-$K_2SiO_3$ NPs, as shown in Fig. 5(d). According to the full scanned spectra, the binding energies of silica, carbon, potassium, oxygen, and sodium were found in all three samples, which are centered at around 101.3 eV, 287.5 eV, 293.2 eV, 531.2 eV, and 976.7eV, respectively. Two signals were obtained for silica as Si2p and Si2s situated at 102.2 eV and 153.6 eV, respectively. The deconvolution of the Si2p spectrum of all these three biomass is shown in Figs. 6(A1-A3). Three sub-signals of Si-O-Si, C-O-H, and C=O corresponding to the binding energy centered at 532.01 eV, 530.01 eV, and 529.01 eV, respectively, confirmed the presence of hybrid silica. As per the XPS analysis, K has a similar asymmetry. The signals of potassium were found to be split into two peaks K2s and K2p, at a binding energy of 378.2 eV and 293.1eV due to spin-orbital interaction, respectively. Figs. 6(B1-B3) show the sub-signals of K2p at 292.5 eV, and 295.5 eV characteristic for $K2p_{3/2}$ and $K2p_{1/2}$, respectively, where silica ironically coordinated the potassium (Tolj *et al*. 2021). The intensity and the area under the curve of Si2p peak for s-$K_2SiO_3$ NPs is relatively increased from other p-$K_2SiO_3$ and w-$K_2SiO_3$ NPs, which implies that the concentration of related silica in SBA is higher, as shown in Figs. 6(C1-C3). From Fig. 6(C2), the Si2p peak of s-$K_2SiO_3$ is broader because of the variation in electron density at the silicon atom by changing the chemical environment (Simonsen *et al*. 2009). Here $Si2p_{1/2}$ and $Si2p_{3/2}$ signal peaks are overleaped due to the Si-OH group being detected as the broadening of the signal of Si2p, which makes it hard to separate the Si-OH group from the Si-O-Si bond for the network of bulk silica (Simonsen *et al*. 2009). By the calculation, the elemental composition for O1s, C1s, Si2p, and K2p of s-$K_2SiO_3$ NPs was found to be 37.02%, 20.18%, 7.79%, and 31.80%, respectively (Table 3).

A fraction of 3.18% of Na1s was present in all samples, possibly due to the chemical process. Meanwhile, we have calculated the direct energy bandgap, $E_g$ by XPS O1s data of p-$K_2SiO_3$, s-$K_2SiO_3$, and w-$K_2SiO_3$ NPs shown in the Figs. 6(D1-D3). Many scientists have reported direct bandgap by XPS O1s data (Kamimura *et al*. 2014, Nichols *et al*. 2014, Zhang *et al*. 2014). The values of $E_g$ were determined as 3.88 eV, 3.79 eV, and 3.78 eV for p-$K_2SiO_3$, s-$K_2SiO_3$, and w-$K_2SiO_3$ NPs, respectively. The estimated

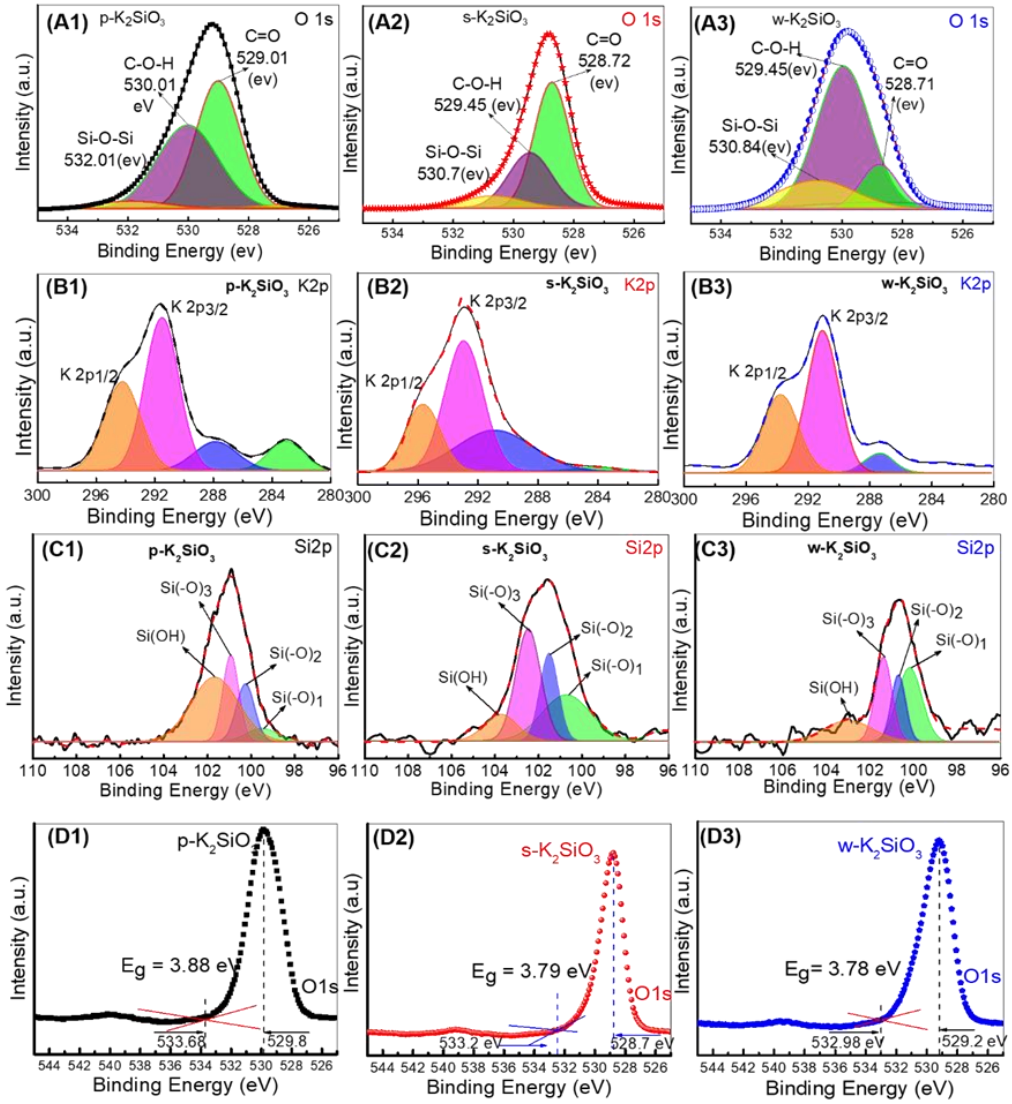


Fig. 6 Core-level analysis of (A, 1-3) O1s, (B, 1-3) K2p, and (C, 1-3) Si2p, (D, 1-3) the determination of $E_g$ through the O1s peak analysis by XPS measurement for w-$K_2SiO_3$, p-$K_2SiO_3$, and s-$K_2SiO_3$ NPs

Table 3: Elemental (atomic) percentage of O, C, Na, Si, and K in s-$K_2SiO_3$ NPs (as per XPS analysis)

| Peak | Intensity (I) | Sensitivity (S) | I/S | Concentration | Concentration (%) |
|---|---|---|---|---|---|
| O 1s | 440,000 | 0.63 | 698,412 | 0.3702 | 37.02 |
| C 1s | 78,048 | 0.205 | 380,721 | 0.2018 | 20.18 |
| Na 1s | 150,747 | 2.51 | 60,058 | 0. 0318 | 3.18 |
| Si 2p | 25,000 | 0.17 | 147,058 | 0.0779 | 7.79 |
| K 2p | 329,895 | 0.55 | 600,000 | 0.3180 | 31.80 |
| | | | $\sum \frac{I}{S} = \mathbf{1,886,258}$ | | |

direct bandgap from XPS was observed in close agreement with the calculated values from Tauc's plot. (Ma *et al.* 2019).

### *3.4 Antibacterial activity*

The antibacterial activity of w-$K_2SiO_3$, p-$K_2SiO_3$, and s-$K_2SiO_3$ NPs was performed on Gram-negative *E. coli* and Gram-positive *S. aureus* bacteria. The antibacterial activity of three synthesized samples of $K_2SiO_3$ was studied through a time-dependent test, as reported by Sharma *et al.* (2015). All three synthesized $K_2SiO_3$ NPs are found to be highly toxic against *E. coli* and *S. aureus* and efficiently inhibit the growth of both organisms. In this study, s-$K_2SiO_3$ NPs displayed the best antibacterial activity compared to p-$K_2SiO_3$ NPs and w-$K_2SiO_3$ NPs (Figs. 7(a) and (b)). A semi-

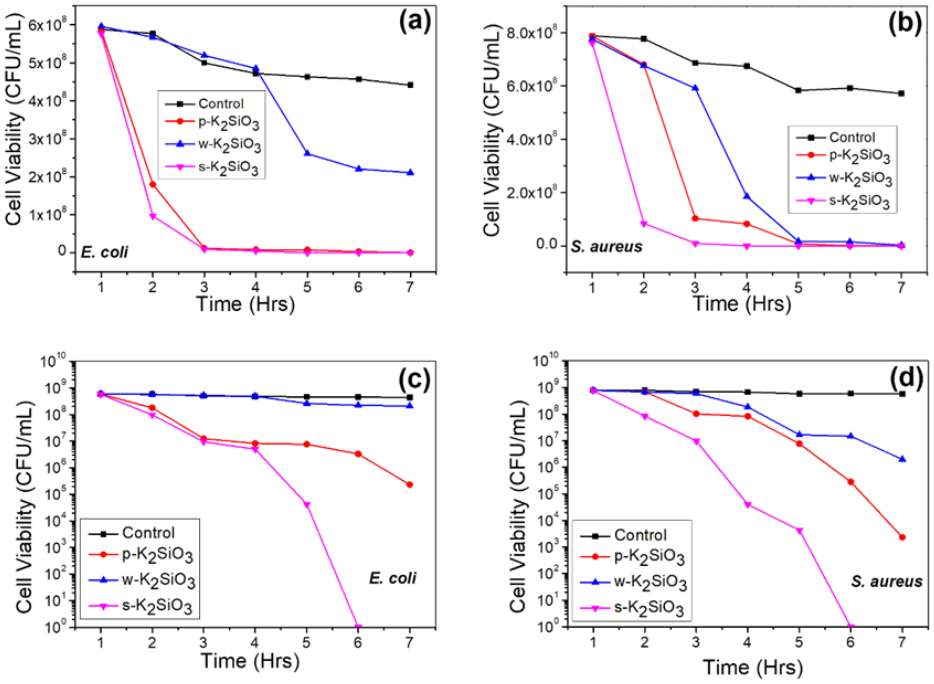


Fig. 7 Time-dependent bacterial cell viability compared with control (without treatment) for (a) *E. coli* and (b) *S. aureus*, and semi-logarithmic graph of the viable cell counts of (c) *E. coli* and (d) *S. aureus* under the treatment of p-$K_2SiO_3$, w-$K_2SiO_3$, and s-$K_2SiO_3$ NPs

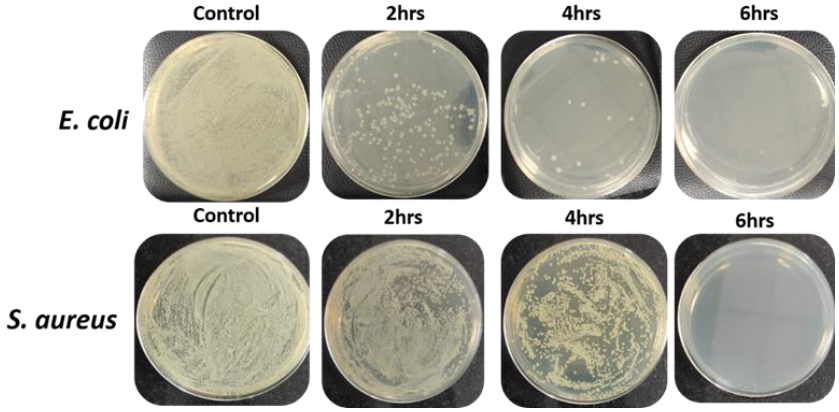


Fig. 8 Culture plates exposed with 0.1 mg of s-$K_2SiO_3$, nanoparticles for 6 h were plated on Luria-Bertani (LB) agar plates for *E. coli* and *S. aureus*

logarithmic graph of the viable cell counts of s-$K_2SiO_3$ NPs in *E. coli* and *S. aureus* displayed the complete eradication in the viable cell counts after 6 h of the treatment. However, the p-$K_2SiO_3$ and w-$K_2SiO_3$ NPs did not completely eradicate the bacterial cell viability for both organisms (Figs. 7(c) and (d)). Fig. 8 shows the culture plates, which confirmed the reduction of colony numbers with time for both *E. coli* and *S. aureus* under the influence of s-$K_2SiO_3$ NPs.

Previous studies demonstrated that the inhibition of bacterial growth was observed to be varied and size-dependent (Balaz *et al*. 2019). The smaller crystallite size leads to direct interactions with microorganisms, which showed more significant effects on both microbes (Ohira and Yamamoto 2012, Li, Wu *et al*. 2016). Compared to the p-$K_2SiO_3$ (53 nm) and w-$K_2SiO_3$ (73 nm), s-$K_2SiO_3$ NPs (47 nm) showed a significantly higher inhibitory effect against both Gram-negative and Gram-positive bacteria due to the smallest crystallite size. Smaller nanoparticles are known to have larger surface areas that result in direct and increased contact with bacterial cell walls. This interaction further results in increased cellular permeability and membrane dysfunction, significantly inhibiting bacterial growth *via* triggering reactive oxygen species (ROS) generation, enzyme inactivation, and damaging proteins and nucleic acids (Wang *et al*. 2017). Although it is well-known that smaller nanoparticles are more toxic to bacterial cells, some studies claim that larger nanoparticles have more antimicrobial potential, which could be due to other factors, such as surface charge and functional modifications (El Badawy *et al*. 2011) (Fig. 9a). Nevertheless, in this study, since the biogenically as-synthesized small-sized $K_2SiO_3$

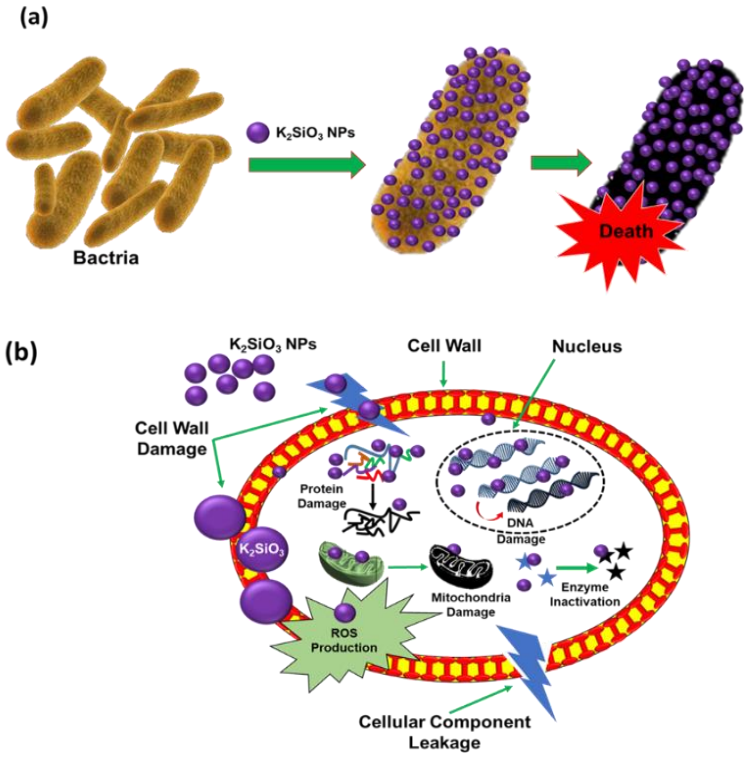


Fig. 9 (a) Schematic diagram of the antibacterial effect of s-$K_2SiO_3$ NPs against bacteria, (b) possible mechanism of antibacterial activity with $K_2SiO_3$ NPs

NPs showed high antimicrobial activity, it can be assumed that small-sized $K_2SiO_3$ NPs might possess more interactive properties with the bacterial cell wall that facilitates enhanced cellular penetration of the $K_2SiO_3$ NPs to initiate the antibacterial activity and the destruction of the cell wall, *via* intercellular ROS generation, inactivation of cellular enzymes, mitochondrial damage, and denaturation of DNA and protein. Consequently, the synthesized s-$K_2SiO_3$ NPs show promising results for their biological applications, primarily as antibacterial agents. The possible mechanism of bacterial destruction by $K_2SiO_3$ NPs is shown in Fig. 9(b). The factors contributing to the remarkable anti-bacterial activity of $K_2SiO_3$ NPs are the significant adhesion to the bacterial cell walls and the release of K+ ions, which results in the formation of hydroxyl ions that cause toxicity to the bacteria and cell membrane. However, further research is needed to fully understand the antibacterial mechanisms of $K_2SiO_3$ NPs synthesized from biomass wastes with underlying effects for enhanced antibacterial capabilities.

## 4. Conclusions

Biogenic w-$K_2SiO_3$, p-$K_2SiO_3$, and s-$K_2SiO_3$ NPs were synthesized by ambient fiery and KOH-assisted thermal process at a precise temperature of 700 °C in a muffle furnace. The dominant peak (113) in the XRD pattern of potassium silicate NPs indicated the breakage of the potassium and silica components regardless of activation temperature. W-H method reveals the micro-strain increased from 0.087 to 0.166 MPa as the crystalline size decreased from 138 to 78 nm for samples varied from w-$K_2SiO_3$ to s-$K_2SiO_3$ NPs, respectively. Electron diffraction rings of the SEAD pattern also confirmed the polycrystalline nature of samples of $K_2SiO_3$ NPs. Agglomerated species of w-$K_2SiO_3$, p-$K_2SiO_3$, and s-$K_2SiO_3$ NPs were confirmed from SEM images. The optical bandgap of w-$K_2SiO_3$, p-$K_2SiO_3$, and s-$K_2SiO_3$ NPs was calculated to be 3.66 eV, 3.75 eV, and 3.78 eV, respectively. The higher optical bandgap values are responsible for the smaller particle size of potassium silicates. The core-level XPS spectra of Si2p deconvolution peaks were observed in the hybrid silica. $K2p_{3/2}$ (292.5 eV) and $K2p_{1/2}$ (295.5 eV) peaks overlap and make the K2p signal because the K is ironically coordinated by silica. The coordination K2p confirms the presence of potassium silicate in all samples. The antibacterial activity of w-$K_2SiO_3$, p-$K_2SiO_3$, and s-$K_2SiO_3$ NPs was investigated against E. coli and S. aureus. In our study, the synthesized s-$K_2SiO_3$ NPs are found to be highly toxic against E. coli and S. aureus compared to p-$K_2SiO_3$ NPs and w-$K_2SiO_3$ NPs were able to eradicate both microorganisms within 6 h of treatment entirely. The findings revealed the novel low-cost development of $K_2SiO_3$ NPs with potent antibacterial activities.

## Acknowledgement

Anirudh Kumar acknowledges the CSIR-SRF (08/096-0012/2020/EMR-I) provided for the Ph.D. dissertation work. Vikas Kumar acknowledges the Centre of Excellence Project to provide the Research Associate fellowship.

Sanjeev K. Sharma (SKS) acknowledges the financial support from the Department of Higher Education, Government of Uttar Pradesh, India for sanctioning the projects (108/2021/2585/Sattar-4-2021-4(28)/2021/20) under the Research & Development program and (78/2022/1984/ Sattar-4-2022-003-70-4099/7/022/19) under Centre of Excellence for Research and innovation of smart materials for Sensor applications. SKS also acknowledges the financial support from the sanctioned project, CST/D-1524, by CST-UP, and C.C.S. University-funded project (Ref. No. Dev./ 1043/29.06.2022) to implement research and innovation. Ashish R. Sharma: This study was supported by the Basic Science Research Program through the National Research Foundation of Korea (NRF) funded by the Ministry of Education (NRF-2020R1C1C1008694).

## References

Ao, W., Fu, J., Mao, X., Wahab, N., Ran, C., Kang, Q., Liu, Y., Jiang, Z., Dai, J. and Bi, X. (2021), "Characterization and analysis of activated carbons prepared from furfural residues by microwave-assisted pyrolysis and activation", *Fuel Proc. Technol*., **213**, 106640. https://doi.org/10.1016/j.fuproc.2020.106640

Asyikin, A.S., Halimah, M.K., Latif, A.A., Faznny, M.F. and Nazrin, S.N. (2020), "Physical, structural and optical properties of bio-silica borotellurite glass system doped with samarium oxide nanoparticles", *J. Non-Cryst. Solids*, **529**, 119777. https://doi.org/10.1016/j.jnoncrysol.2019.119777

Azlan, M.N., Halimah, M.K., Shafinas, S.Z. and Daud, W.M. (2014), "Polarizability and optical basicity of Er3+ ions doped tellurite based glasses", *Chalcogen. Lett*., **11**(7), 319-335.

Balaz, M., Balazova, L., Kovacova, M., Daneu, N., Salayova, A., Bedlovicova, Z. and Tkacikova, L. (2019), "The relationship between precursor concentration and antibacterial activity of biosynthesized Ag nanoparticles", *Adv. Nano Res*., **7**(2), 125-134. https://doi.org/10.12989/ANR.2019.7.2.125

Bhat, J.A., Shivaraj, S.M., Singh, P., Navadagi, D.B., Tripathi, D.K., Dash, P.K., Solanke, A.U., Sonah, H. and Deshmukh, R. (2019), "Role of silicon in mitigation of heavy metal stresses in crop plants", *Plants*, **8**(3), 71-91. https://doi.org/10.3390/plants8030071

Billingham, J., Breen, C. and Yarwood, J. (1997), "Adsorption of polyamine, polyacrylic acid and polyethylene glycol on montmorillonite: An in situ study using ATR-FTIR", *Vib. Spectrosc*., **14**(1), 19-34. https://doi.org/10.1016/S0924-2031(96)00074-4

Bogireddy, N.K.R., Gomez, L.M., Osorio-Roman, I. and Agarwal, V. (2017), "Synthesis of gold nanoparticles using Coffea Arabica fruit extract", *Adv. Nano Res*., **5**(3), 253-260. https://doi.org/10.12989/ANR.2017.5.3.253

Carlisle, E.M. (1986), "Silicon as an essential trace element in animal nutrition", *Ciba Found. Symp*., **121**, 123-139. https://doi.org/10.1002/9780470513323.ch8

Chen, A., Mu, W. and Chen, Y. (2014), "Compressive elastic moduli and polishing performance of non-rigid core/shell structured PS/SiO2 composite abrasives evaluated by AFM", *Appl. Surf. Sci.*, **290**, 433-439. https://doi.org/10.1016/j.apsusc.2013.11.100

Dallagnol, L.J., Rodrigues, F.A., Pascholati, S.F., Fortunato, A.A. and Camargo, L.E.A. (2015), "Comparison of root and foliar applications of potassium silicate in potentiating post-infection defences of melon against powdery mildew", *Plant Pathol*., **64**(5), 1085-1093. https://doi.org/10.1111/ppa.12346

Danchin, A. and Nikel, P.I. (2019), "Why nature chose potassium", *J. Mol. Evol*., **87**(9-10), 271-288. https://doi.org/10.1007/s00239-019-09915-2

de Oliveira, K.G., de Lima, R.R.S., de Longe, C., Bicudo, T.d.C., Sales, R.V. and de Carvalho, L.S. (2022), "Sodium and potassium silicate-based catalysts prepared using sand silica concerning biodiesel production from waste oil", *Arab. J. Chem*., **15**(2), 103603. https://doi.org/10.1016/j.arabjc.2021.103603

Deng, W., Kang, T., Liu, H., Zhang, J., Wang, N., Lu, N., Ma, Y., Umar, A. and Guo, Z. (2018), "Potassium hydroxide activated and nitrogen doped graphene with enhanced supercapacitive behavior", *Sci. Adv. Mater*., **10**(7), 937-949. https://doi.org/10.1166/sam.2018.3279

Deshmukh, R.K., Ma, J.F. and Bélanger, R.R. (2017), "Role of silicon in plants", *Front. Plant Sci*., **8**, 1858. https://doi.org/10.3389/fpls.2017.01858

Dogan, M.F., Yildiz, O., Arslan, S.O. and Ulusoy, K.G. (2019), "Potassium channels in vascular smooth muscle: A patho-physiological and pharmacological perspective", *Fundam. Clin. Pharmacol*., **33**(5), 504-523. https://doi.org/10.1111/fcp.12461

Dousti, M.R., Sahar, M.R., Ghoshal, S.K., Amjad, R.J. and Samavati, A.R. (2013), "Effect of AgCl on spectroscopic properties of erbium doped zinc tellurite glass", *J. Mol. Struct*., **1035**, 6-12. https://doi.org/10.1016/j.molstruc.2012.09.023

El Badawy, A.M., Silva, R.G., Morris, B., Scheckel, K.G., Suidan, M.T. and Tolaymat, T.M. (2011), "Surface charge-dependent toxicity of silver nanoparticles", *Environ. Sci. Technol*., **45**(1), 283-287. https://doi.org/10.1021/es1034188

Epstein, E. (2009), "Silicon: its manifold roles in plants", *Ann. Appl. Biol*., **155**(2), 155-160. https://doi.org/10.1111/j.1744-7348.2009.00343.x

França, A.A., Schultz, J., Borges, R., Wypych, F. and Mangrich, A.S. (2017), "Rice husk ash as raw material for the synthesis of silicon and potassium slow-release fertilizer", *J. Brazil. Chem. Soc*., **28**, 2211-2217. http://doi.org/10.21577/0103-5053.20170072

Gandolfi, M.G., Pagani, S., Perut, F., Ciapetti, G., Baldini, N., Mongiorgi, R. and Prati, C. (2008), "Innovative silicate-based cements for endodontics: A study of osteoblast-like cell response", *J. Biomed. Mater. Res. A.*, **87**(2), 477-486. http://doi.org/10.1002/jbm.a.31795

Ghiasi Moaser, A., Afkham, A.G., Khoshnavazi, R. and Rostamnia, S. (2023), "Nickel substituted polyoxometalates in layered double hydroxides as metal-based nanomaterial of POM-LDH for green catalysis effects", *Sci. Rep*., **13**(1), 4114. https://doi.org/10.1038/s41598-023-31356-7

Gong, H.S. and Kim, H.G. (2013), "Formation and photo-luminescence of Y2O3-H3BO3: Eu3+ powders by mechanical alloying", *Curr. Appl. Phys*., **13**(3), 453-456. https://doi.org/10.1016/j.cap.2012.09.005

Halimah, M.K., Daud, W.M., Sidek, H.A.A., Zaidan, A.W. and Zainal, A.S. (2010), "Optical properties of ternary tellurite glasses", *Mater. Sci. Pol*., **28**(1), 173-180.

He, F.J. and MacGregor, G.A. (2008), "Beneficial effects of potassium on human health", *Physiol. Plant*., **133**(4), 725-735. https://doi.org/10.1111/j.1399-3054.2007.01033.x

Hongwen, M.A., Jing, Y., Shuangqing, S.U., Meitang, L.I.U., Hong, Z., Yingbin, W., Hongbin, Q.I., Pan, Z. and Wengui, Y.A.O. (2015), "20 years advances in preparation of potassium salts from potassic rocks: a review", *Acta Geol. Sin*., **89**(6), 2058-2071. https://doi.org/10.1111/1755-6724.12617

Hu, L., Wu, H., Zhu, T., Fu, C., He, J., Ying, P. and Zhao, X. (2015), "Tuning multiscale microstructures to enhance thermo-electric performance of n-type Bismuth-Telluride-based solid solutions", *Adv. Energy Mater*., **5**(17), 1500411. https://doi.org/10.1002/aenm.201500411

Imran, M., Shahzad, K., Munir, S., Wasim, M. and Hussnain, A. (2020), "Synthesis and characterization of potassium silicate fertilizer using fly ashes of bituminous and sub-bituminous and lignite coal", *J. Pak. Int. Chem. Eng.*, **48**(2), 47-54. https://doi.org/10.54693/piche.04826

Jawad, A.H. and Abdulhameed, A.S. (2020), "Statistical modeling of methylene blue dye adsorption by high surface area mesoporous activated carbon from bamboo chip using KOH-assisted thermal activation", *Energy Ecol. Environ.*, **5**(6), 456-469. https://doi.org/10.1007/s40974-020-00177-z

Jones, L.H.P. and Handreck, K.A. (1967), "Silica in soils, plants, and animals", *Adv. Agron.*, **19,** 107-149. https://doi.org/10.1016/S0065-2113(08)60734-8

Jurkić, L.M., Cepanec, I., Pavelić, S.K. and Pavelić, K. (2013), "Biological and therapeutic effects of ortho-silicic acid and some ortho-silicic acid-releasing compounds: New perspectives for therapy", *Nutr. Metab.*, **10**, 1-12. https://doi.org/10.1186/1743-7075-10-2

Kamimura, T., Sasaki, K., Hoi Wong, M., Krishnamurthy, D., Kuramata, A., Masui, T., Yamakoshi, S. and Higashiwaki, M. (2014), "Band alignment and electrical properties of Al2O3/β-Ga2O3 heterojunctions", *Appl. Phys. Lett.*, **104**(19), 192104. https://doi.org/10.1063/1.4876920

Kang, H.G., Jeong, J.M., Hong, S.B., Lee, G.Y., Kim, J.W. and Choi, B.G. (2019), "Scalable exfoliation and activation of graphite into porous graphene using microwaves for high-performance supercapacitors", *J. Alloys Compd.*, **770**, 458-465. https://doi.org/10.1016/j.jallcom.2018.08.042

Kumar, A. and Mohanty, T. (2014), "Electro-optic modulation induced enhancement in photocatalytic activity of N-doped TiO2 thin films", *J. Phys. Chem. C*, **118**(13), 7130-7138. https://doi.org/10.1021/jp4103977

Kumar, S., Sahay, L.K., Jha, A.K. and Prasad, K. (2013), "Synthesis and characterization of nanocrystalline Al0.5Ag0.5 TiO3 powder", *Adv. Nano Res.*, **1**(4), 211-218. https://doi.org/10.12989/ANR.2013.1.4.211

Kumchompoo, J. and Puntharod, R. (2022), "Synthesis and characterization of lithium silicate and potassium silicate from rice husk ash by hydrothermal-microwave method and application for biodiesel catalyst", *Suranaree J. Sci. Technol.*, **29**(3), 1-7.

Li, M., Wu, W., Qiao, R., Tan, L., Li, Z. and Zhang, Y. (2016), "Ag-decorated Fe3O4@ SiO2 core-shell nanospheres: seed-mediated growth preparation and their antibacterial activity during the consecutive recycling", *J. Alloys Compd.*, **676**, 113-119. https://doi.org/10.1016/j.jallcom.2016.03.191

Li, Y., Zeng, G., Yang, G., Wu, Q., Zhang, H., Li, W. and Qian, Y. (2019), "Synthesis, characterization and properties of ATO/ potassium silicate film prepared by twice spray pyrolysis", *J. Alloys Compd.*, **772**, 240-246. https://doi.org/10.1016/j.jallcom.2018.09.016

Ma, H.P., Yang, J.H., Yang, J.G., Zhu, L.Y., Huang, W., Yuan, G.J., Feng, J.J., Jen, T.C. and Lu, H.L. (2019), "Systematic study of the SiOx film with different stoichiometry by plasma-enhanced atomic layer deposition and its application in SiOx/ SiO2 super-lattice", *Nanomaterials*, **9**(1), 55. https://doi.org/10.3390/nano9010055

Mason, B. (1966), "Composition of the Earth", *Nature*, **211**, 616-618. https://doi.org/10.1038/211616a0

Mastalska-Popławska, J., Izak, P., Góral, Z. and Stempkowska, A. (2020), "Rheological parameters of polymer-silicate gels", *J. Phys. Conf. Ser.*, **1527**, 012035. https://doi.org/10.1088/1742-6596/1527/1/012035

Menzies, J., Bowen, P., Ehret, D. and Glass, A.D.M. (1992), "Foliar applications of potassium silicate reduce severity of powdery mildew on cucumber, muskmelon, and zucchini squash", *J. Am. Soc. Hortic. Sci.*, **117**(6), 902-905. https://doi.org/10.21273/JASHS.117.6.902

Mughal, B., Zaidi, S.Z.J., Zhang, X. and Hassan, S.U. (2021), "Biogenic nanoparticles: Synthesis, characterisation and applications", *Appl. Sci.*, **11**(6), 2598. https://doi.org/10.3390/app11062598

Nandiyanto, A.B.D., Permatasari, N., Sucahya, T.N., Abdullah, A.G. and Hasanah, L. (2017), "Synthesis of potassium silicate nanoparticles from rice straw ash using a flame-assisted spray-pyrolysis method", *IOP Conf. Ser. Mater. Sci. Eng.*, **180**, 012133. https://doi.org/10.1088/1757-899X/180/1/012133

Nichols, M.T., Li, W., Pei, D., Antonelli, G.A., Lin, Q., Banna, S., Nishi, Y. and Shohet, J.L. (2014), "Measurement of bandgap energies in low-k organosilicates", *J. Appl. Phys.*, **115**(9), 094105. https://doi.org/10.1063/1.4867644

Ohira, T. and Yamamoto, O. (2012), "Correlation between antibacterial activity and crystallite size on ceramics", *Chem. Eng. Sci.*, **68**(1), 355-361. https://doi.org/10.1016/j.ces.2011.09.043

Pandey, G.K. and Mahiwal, S. (2020), *Role of Potassium in Plants*, Springer, New York, U.S.A.

Pascal, C., Pascal, J.L., Favier, F., Elidrissi Moubtassim, M.L. and Payen, C. (1999), "Electrochemical synthesis for the control of γ-Fe2O3 nanoparticle size. Morphology, microstructure, and magnetic behavior", *Chem. Mater.*, **11**(1), 141-147. https://doi.org/10.1021/cm980742f

Pędziwiatr-Werbicka, E., Miłowska, K., Podlas, M., Marcinkowska, M., Ferenc, M., Brahmi, Y., Katir, N., Majoral, J.P., Felczak, A. and Boruszewska, A. (2014), "Oleochemical-tethered SBA-15-type silicates with tunable nanoscopic order, carboxylic surface, and hydrophobic framework: cellular toxicity, hemolysis, and antibacterial activity", *Chem. Eur. J.*, **20**(31), 9596-9606. https://doi.org/10.1002/chem.201402583

Permatasari, N., Sucahya, T.N. and Nandiyanto, A.B.D. (2016), "Agricultural wastes as a source of silica material", *Indones. J. Sci. Technol.*, **1**(1), 82-106. https://doi.org/10.17509/ijost.v1i1.2216

Reddy, R.R., Ahammed, Y.N., Gopal, K.R. and Raghuram, D.V. (1998), "Optical electronegativity and refractive index of materials", *Opt. Mater.*, **10**(2), 95-100. https://doi.org/10.1016/S0925-3467(97)00171-7

Sharma, S.K., Pamidimarri, D.V.N.S., Kim, D.Y. and Na, J.G. (2015), "Y-doped zinc oxide (YZO) nanoflowers, micro-structural analysis and test their antibacterial activity", *Mater. Sci. Eng. C*, **53**, 104-110. https://doi.org/10.1016/j.msec.2015.04.007

Simonsen, M.E., Sønderby, C., Li, Z. and Søgaard, E.G. (2009), "XPS and FT-IR investigation of silicate polymers", *J. Mater. Sci.*, **44**, 2079-2088. https://doi.org/10.1007/s10853-009-3270-9

Sommer, S., Raidt, T., Fischer, B.M., Katzenberg, F., Tiller, J.C. and Koch, M. (2016), "THz-spectroscopy on high density polyethylene with different crystallinity", *J. Infrared Millim. Terahertz Waves*, **37**, 189-197. https://doi.org/10.1007/s10762-015-0219-8

Tallury, P., Payton, K. and Santra, S. (2008), "Silica-based multimodal/multifunctional nanoparticles for bioimaging and biosensing applications", *Nanomedicine*, **3**(4), 579-92. https://doi.org/10.2217/17435889.3.4.579.

Tamuly, J., Bhattacharjya, D. and Saikia, B.K. (2022), "Graphene/ graphene derivatives from coal, biomass, and wastes: Synthesis, energy applications, and perspectives", *Energ. Fuel.*, **36**(21), 12847-12874. https://doi.org/10.1021/acs.energyfuels.2c00976

Tannen, R.L. (1983), "Effects of potassium on blood pressure control", *Ann. Intern. Med.*, **98**(5 Part 2), 773-780. https://doi.org/10.7326/0003-4819-98-5-773

Tolj, D., Ivšić, T., Živković, I., Semeniuk, K., Martino, E., Akrap, A., Reddy, P., Klebel-Knobloch, B., Lončarić, I. and Forró, L.

(2021), "Synthesis of murunskite single crystals: A bridge between cuprates and pnictides", *Appl. Mater. Today.*, **24**, 101096. https://doi.org/10.1016/j.apmt.2021.101096

Van Horn, D.J., Van Horn, M.L., Barrett, J.E., Gooseff, M.N., Altrichter, A.E., Geyer, K.M., Zeglin, L.H. and Takacs-Vesbach, C.D. (2013), "Factors controlling soil microbial biomass and bacterial diversity and community composition in a cold desert ecosystem: role of geographic scale", *PLoS One*, **8**(6), e66103. https://doi.org/10.1371/journal.pone.0066103

Venkatraman, S.K. and Swamiappan, S. (2020), "Review on calcium-and magnesium-based silicates for bone tissue engineering applications", *J. Biomed. Mater. Res. A*, **108**(7), 1546-1562. https://doi.org/10.1002/jbm.a.36925

Walker, A.J. and Whitehead, N. (1966), "Differences in molecular species present in aqueous potassium silicate solutions and their efficiency as adhesives for phosphors on glass", *J. Appl. Chem.*, **16**(8), 230-238. https://doi.org/10.1002/jctb.5010160804

Wang, L., Hu, C. and Shao, L. (2017), "The antimicrobial activity of nanoparticles: Present situation and prospects for the future", *Int. J. Nanomed.*, **12**, 1227-1249. https://doi.org/10.2147/IJN.S121956

Wang, M., Zheng, Q., Shen, Q. and Guo, S. (2013), "The critical role of potassium in plant stress response", *Int. J. Mol. Sci.*, **14**(4), 7370-7390. https://doi.org/10.3390/ijms14047370

Wu, B.C., Wei, C.K., Hsueh, N.S. and Ding, S.J. (2015), "Comparative cell attachment, cytotoxicity and antibacterial activity of radiopaque dicalcium silicate cement and white-coloured mineral trioxide aggregate", *Int. Endod. J.*, **48**(3), 268-276. https://doi.org/10.1111/iej.12310.

Wu, L. and Liu, M. (2007), "Slow-release potassium silicate fertilizer with the function of superabsorbent and water retention", *Ind. Eng. Chem. Res.*, **46**(20), 6494-6500. https://doi.org/10.1021/ie070573l

Xu, Y., Chang, L. and Hu, Y.H. (2017), "KOH-assisted microwave post-treatment of activated carbon for efficient symmetrical double-layer capacitors", *Int. J. Energy Res.*, **41**(5), 728-735. https://doi.org/10.1002/er.3676

Youssry, S.M., Abd Elkodous, M., Kumar, R., Kawamura, G., Tan, W.K. and Matsuda, A. (2023), "Thermal-assisted synthesis of reduced graphene oxide-embedded Ni nanoparticles as high-performance electrode material for supercapacitor", *Electrochim. Acta*, **463**, 142814. https://doi.org/10.1016/j.electacta.2023.142814

Zeng, H., Li, Z., Cai, W., Cao, B., Liu, P. and Yang, S. (2007), "Microstructure control of Zn/ZnO core/shell nanoparticles and their temperature-dependent blue emissions", *J. Phys. Chem. B*, **111**(51), 14311-14317. https://doi.org/10.1021/jp0770413

Zhang, F., Saito, K., Tanaka, T., Nishio, M., Arita, M. and Guo, Q. (2014), "Wide bandgap engineering of (AlGa) 2O3 films", *Appl. Phys. Lett.*, **105**(16), 162107. https://doi.org/10.1063/1.4900522

Zhu, Y.J., Guo, X.X. and Sham, T.K. (2017), "Calcium silicate-based drug delivery systems", *Expert Opin. Drug Deliv.*, **14**(2), 215-228. https://doi.org/10.1080/17425247.2016.1214566

*CC*